

Colossal Terahertz Magnetoresistance from Magnetic Polarons in EuZn_2P_2

E. Marulanda,¹ M. Dutra,² N. M. Kawahala,¹ E. D. Stefanato,¹ G. Vasques,² J. Munevar,³ M. A. Avila,² and F. G. G. Hernandez^{1,*}

¹*Instituto de Física, Universidade de São Paulo, 05508-090, São Paulo, SP, Brazil*

²*CCNH, Universidade Federal do ABC, 09210-580, Santo André, SP, Brazil*

³*Departamento de Física, Universidad del Valle, A. A. 25360, Cali, Colombia*

(Dated: March 24, 2026)

Magnetic polarons can generate colossal magnetoresistance in magnetic semiconductors, yet their terahertz electro-dynamics remain largely unexplored. Here we report magneto-terahertz spectroscopy of the Eu-based Zintl antiferromagnet EuZn_2P_2 . The low-frequency conductivity shows pronounced non-Drude behavior consistent with an evolution from isolated to overlapping magnetic polarons upon cooling. The polaron relaxation time reaches a maximum at the Néel temperature and exhibits a strong magnetic-field dependence. This polaron-driven reshaping of the conductivity leads to a strongly frequency-dependent magnetoresistance that becomes colossal in the terahertz range, reaching about 90 % at 1.5 THz, roughly three times larger than the zero-frequency limit value. These results demonstrate that magnetic polarons strongly govern the low-energy electro-dynamics and highlight the sensitivity of terahertz spectroscopy to polaronic magnetotransport in correlated magnetic semiconductors.

Introduction—Eu-based Zintl phases have emerged as a platform where strong local moments can coexist with low carrier density and narrow gaps, enabling colossal magnetoresistance (CMR) without the mixed valence and perovskite chemistry characteristic of manganites [1–7]. In several members of this family, CMR has been linked to magnetic polarons—charge carriers dressed by ferromagnetically aligned spin clouds whose growth and overlap on cooling or under externally applied magnetic fields strongly renormalize charge transport [1, 2, 8–10]. A key open question is how magnetic-polaron transport manifests in the terahertz electro-dynamics, where conductivity probes carrier dynamics on picosecond timescales and can reveal relaxation processes and bound states inaccessible to direct current (dc) measurements [11, 12].

EuZn_2P_2 is a trigonal (CaAl_2Si_2 -type) Zintl antiferromagnet with A-type order below the Néel temperature $T_N \approx 23.5$ K [13]. Its resistivity shows an insulating-like upturn on cooling [14] and a strong negative magnetoresistance (MR) that reduces the low-temperature resistivity by several orders of magnitude [15]. Recent transport, electron spin resonance (ESR), and thermodynamic measurements support a magnetic-polaron scenario [16]. However, while EuZn_2P_2 has been extensively studied by dc transport and optical spectroscopy [15, 16], magneto-terahertz measurements on pristine crystals remain largely unexplored. Terahertz time-domain spectroscopy (THz-TDS) [17, 18] provides contact-free access to the complex conductivity in the spectral window where itinerant carriers and low-energy excitations compete [19, 20]. Our recent study of Ga-substituted EuZn_2P_2 at room temperature revealed a pronounced enhancement of the low-frequency electronic response and an increased scattering time, demonstrating the sensitivity of THz-TDS to changes in carrier density and mo-

mentum relaxation in this material [21].

In this Letter we present a magneto-terahertz spectroscopy study of pristine single crystals of EuZn_2P_2 across 1.6–150 K in magnetic fields up to 7 T. By parameterizing the low-frequency conductivity we extract its characteristic scales and effective relaxation time, revealing successive regimes consistent with the evolution from isolated to overlapping magnetic polarons and their persistence below T_N . We further quantify the frequency dependence of the MR and show that it becomes colossal at terahertz frequencies, remaining strongly enhanced relative to the zero-frequency limit of the response even above T_N . These results establish terahertz electro-dynamics as a powerful probe of magnetic-polaron transport, providing a direct spectroscopic route to identify their coexistence and dynamics and to uncover colossal magnetoresistance in correlated magnetic semiconductors.

Results—We measure the complex terahertz transmission of EuZn_2P_2 using THz-TDS over the frequency range $\nu = 0.2$ –2.0 THz, temperatures $T = 1.6$ –150 K, and magnetic fields up to $B = 7$ T. The corresponding complex optical conductivity $\sigma(\nu)$ is obtained as described in the Supplementary Material [22]. In the following, we focus on the dissipative (real) component $\sigma_1(\nu)$, which captures the low-energy electronic response relevant to magnetic polarons.

We first present zero-field spectra spanning the temperature range where magnetic-polaron phenomenology has been established in EuZn_2P_2 by transport and local probes [15, 16]. Figure 1(a) shows $\sigma_1(\nu)$ at several representative temperatures. The low-energy response appears as a broad electronic feature whose maximum, near 0.6 THz at high temperatures, shifts to lower frequencies upon cooling, as seen by the progressive displacement of the low-frequency peak in Fig. 1(a). Its

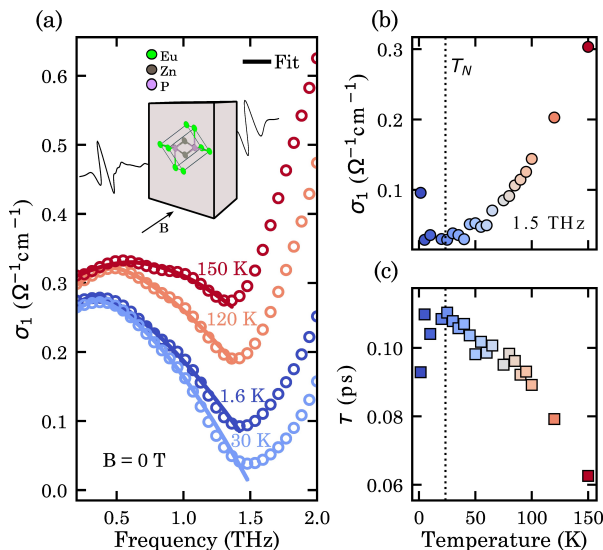


FIG. 1. (a) Real part of the optical conductivity at selected temperatures in zero magnetic field. Solid lines are power-law fits to the low-frequency response below the conductivity minimum. *Inset*: CaAl₂Si₂-type crystal structure and schematic of the magneto-terahertz time-domain spectroscopy in Faraday geometry. (b) Temperature dependence of σ_1 at 1.5 THz, a representative frequency near the conductivity minimum. (c) Effective scattering time extracted from the fits in (a). The dashed line marks the Néel temperature. Error bars are smaller than the data point symbols.

high-frequency side overlaps with the low-frequency tail of a Eu-related phonon mode, producing a pronounced conductivity minimum at $\nu_{\min} \sim 1.5$ THz that marks the boundary between the two contributions. Although the phonon peak at 3 THz lies outside our spectral range [15, 21, 23], this conductivity minimum indicates the interplay between the electronic and phonon responses, which has been shown to influence transport in Eu-based compounds hosting magnetic polarons [24].

To isolate the low-energy electronic contribution, we restrict our analysis to frequencies below ν_{\min} , and parameterize $\sigma_1(\nu)$ with an offset power-law form, $\sigma_1(\nu) = \sigma_p + A(\nu - \nu_0)^{2q}$, consistent with a generalized universal dielectric response [25–27]. Here σ_p sets the low-frequency conductivity baseline, while A , q , and ν_0 describe the non-Drude curvature of the electronic response. Over the measured temperature range, we obtain $A < 0$, $0.7 \leq q \leq 1$, and ν_0 in the range 0.3–0.6 THz (see Supplementary Material [22]).

The fitted offset frequency ν_0 corresponds to the maximum of the electronic feature. Its sub-terahertz scale is far below any established electronic energy scale in EuZn₂P₂. Infrared reflectivity places the indirect and direct gaps at approximately 22 and 80 THz, respectively [15]. Transport measurements yield activation energies that vary with sample and fit window but consistently fall in the 5–42 THz range, with earlier reports

extending to 48–73 THz [3, 16]. Even the magnetic-field-induced gap renormalization, from the A-type antiferromagnetic to the fully polarized configuration, is on the order of 10^2 THz [16]. We therefore interpret ν_0 as a genuine low-energy electronic relaxation scale associated with a dynamical process rather than a conventional electronic excitation, whose origin we relate below to magnetic-polaron dynamics.

Figure 1(b) shows the temperature dependence of σ_1 at $\nu = 1.5$ THz, extracted directly from the measured spectra. Because this frequency lies close to the conductivity minimum in Fig. 1(a), it provides a convenient probe of the high-frequency edge of the electronic feature and its temperature-driven reshaping. Upon cooling, $\sigma_1(\nu = 1.5$ THz) decreases exponentially from roughly $0.3 \Omega^{-1} \text{cm}^{-1}$ at 150 K to nearly zero at lower temperatures, consistent with thermally activated behavior. The Arrhenius plot yields an activation energy of 3.5 ± 0.3 THz for $T > 60$ K (see Supplementary Material [22]), a temperature below which magnetic-polaron correlations have been reported in EuZn₂P₂ [13]. As observed in EuCd₂P₂ [12], the Eu-related phonon response exhibits only weak temperature dependence in the complex optical response of closely related Eu-based compounds. This suggests that the temperature evolution of the conductivity minimum in Fig. 1(a) is primarily driven by changes in the electronic response associated with magnetic-polaron dynamics rather than by modifications of the phonon contribution.

To characterize the relaxation dynamics of the electronic response, we estimate an effective scattering time τ from the spectral width of this feature. Figure 1(c) shows $\tau(T)$, extracted from the fitted spectra, with values in the sub-picosecond range. On cooling from 150 K to ~ 100 K, τ increases, consistent with a progressive reduction of phonon scattering in semiconductors. Between ~ 100 K and T_N , τ continues to increase but with a slope reduced to roughly one-half of its high-temperature value. This regime coincides with the temperature range where the exponent q , which controls the non-Drude curvature of the conductivity, begins to increase, reaching a maximum near 60 K before decreasing again toward T_N (see Supplementary Material [22]). Near T_N , τ reaches a pronounced maximum and decreases again at lower temperatures. The maximum of τ near T_N is consistent with the strong influence of magnetic correlations on relaxation processes associated with magnetic-polaron dynamics, which occurs in sub-picosecond timescales.

Figure 2 shows two conductivity scales extracted from the fits in Fig. 1(a): the dc conductivity $\sigma_{\text{dc}} = \sigma_1(0)$ obtained by extrapolating the power law to zero frequency, and $\sigma_p = \sigma_1(\nu_0)$, corresponding to the conductivity at the peak of the electronic feature. While σ_{dc} reflects the ability of carriers to sustain long-range transport, σ_p captures the magnitude of the electronic response on terahertz time scales. Both quantities evolve nonmono-

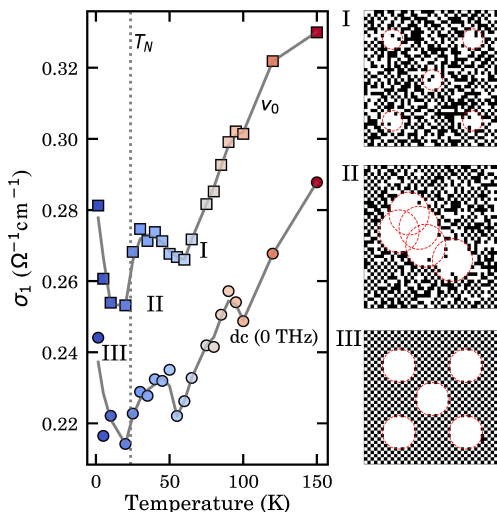


FIG. 2. Optical conductivity at dc (circles) and the low-energy scale σ_p evaluated at ν_0 (squares), extracted from the fits in Fig. 1. Solid lines are guides to the eye. The dashed line marks T_N . *Right panels*: schematic spin-plane snapshots (black: down; white: up) illustrating (I) isolated magnetic polarons, (II) their overlap and connection (percolative transport), and (III) the persistence of polaronic correlations in the antiferromagnetic phase. Error bars are smaller than the data point symbols.

tonically and exhibit distinct slope changes, indicating successive crossovers in the underlying transport regime.

Within the magnetic-polaron scenario, we distinguish three regimes (I–III) in Fig. 2. In regime I ($T \sim 100$ – 60 K), both conductivity scales decrease upon cooling after a subtle increase near ~ 100 K, with σ_{dc} remaining systematically smaller than σ_p , consistent with carrier self-trapping into ferromagnetic clusters. The onset of this regime coincides with the temperature at which $\tau(T)$ first changes slope, as discussed above, and with ESR evidence for local spin-carrier polarization and magnetic-polaron formation in EuZn_2P_2 [13]. In regime II ($T \sim 60$ K– T_N), both σ_{dc} and σ_p initially increase upon cooling, reach a maximum in this interval, and decrease again as T_N is approached, consistent with increasing connectivity of ferromagnetic clusters as they begin to overlap. Finally, in regime III ($T < T_N$), both conductivity scales remain finite and continue to evolve, suggesting that ferromagnetic clusters or polaronic correlations persist against the long-range antiferromagnetic background [28]. Although CMR is rare in antiferromagnetic materials [8, 29], the observed behavior is consistent with reports of ferromagnetic polarons stabilized within antiferromagnetic order in closely related Eu-based materials [30].

We next examine how magnetic fields modify the terahertz conductivity by measuring $\sigma_1(\nu, B)$ at two representative temperatures, 1.6 K and 50 K, below and above T_N . Figure 3(a) shows $\sigma_1(\nu)$ at 1.6 K for selected fields.

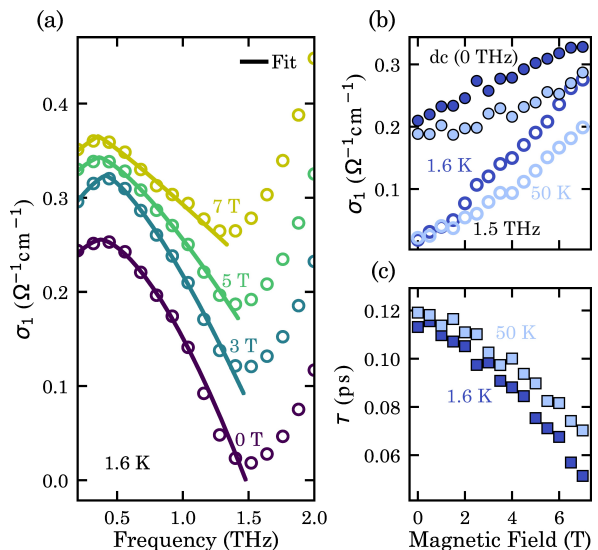


FIG. 3. (a) Optical conductivity at representative magnetic fields. Solid lines are power-law fits to the low-frequency response. (b) Magnetic-field dependence of σ_1 at 0 THz (dc, filled symbols) and at 1.5 THz (open symbols), measured at $T = 1.6$ and 50 K. (c) Effective scattering time extracted from the low-frequency fits in (a), shown at the same temperatures as in (b). Error bars are smaller than the data point symbols.

As B increases, the conductivity minimum is progressively lifted and the curvature of the electronic feature changes. As discussed above, the phonon tail is weak in this spectral range, so the field dependence of the minimum primarily reflects changes in the electronic response. We apply the same low-frequency parameterization used in Fig. 1(a) to the field-dependent spectra. The resulting parameters reveal a systematic field-induced reshaping of the electronic feature. The coefficient A becomes progressively less negative with increasing field at both temperatures. The exponent q starts near 0.8 at zero field but evolves differently at the two temperatures, decreasing toward ~ 0.5 at 1.6 K and increasing to ~ 0.9 at 50 K as B approaches 7 T. By contrast, the offset frequency ν_0 remains within the 0.35–0.5 THz range (see Supplementary Material [22]). These trends indicate that the magnetic field primarily modifies the spectral curvature and amplitude of the electronic response, while leaving its characteristic frequency scale largely unchanged.

Figure 3(b) compares the field dependence of σ_{dc} and $\sigma_1(\nu = 1.5$ THz), both of which increase with increasing B at 1.6 K and 50 K. The relative enhancement is systematically larger at 1.5 THz than in σ_{dc} , indicating a stronger field-induced change in the finite-frequency conductivity than in its zero-frequency extrapolation. Within a magnetic-polaron picture, this behavior is expected because the polaron moment couples directly to the magnetic field and modifies its spatial extent, causing polarons aligned with the field to expand while antiparal-

lel ones contract [31]. Such field-induced changes in the polaron configuration and overlap can enhance the THz conductivity more rapidly than the long-range transport captured by σ_{dc} . The persistence of this contrast at 50 K is consistent with magnetic-polaron correlations extending well above the onset of long-range order in EuZn_2P_2 [15].

Figure 3(c) shows the effective scattering time $\tau(B)$ extracted from the field-dependent fits. At both 1.6 and 50 K, τ decreases with increasing B , with a stronger suppression observed at low temperature. This trend indicates that the field-induced conductivity enhancement discussed above cannot be attributed to an increase in the relaxation time. Instead, the response is consistent with a field-driven increase in the effective mobile fraction and/or a redistribution of low-energy spectral weight associated with magnetic-polaron correlations. A mechanism based on spectral-weight transfer of small polarons was previously reported for changes in the mid-infrared conductivity of CMR manganites [32, 33]. The persistence of this behavior at 50 K further supports the presence of polaronic ferromagnetic correlations above T_N in EuZn_2P_2 [15, 30].

The strong field sensitivity of the conductivity within the magnetic-polaron scenario suggests that the magnetoresistance should exhibit a pronounced frequency dependence in the terahertz range. To quantify this dynamical counterpart of the dc magnetoresistance, we define a conductivity-based terahertz magnetoresistance $\text{MR}(\nu, B) = [\sigma_1(\nu, 0) - \sigma_1(\nu, B)] / \sigma_1(\nu, B)$. Figure 4(a–c) shows MR maps as a function of magnetic field and frequency at 1.6 K, 50 K, and 120 K.

At $T = 1.6$ K (Fig. 4a), negative MR exhibits a pronounced cone-like structure centered near $\nu \sim 1.5$ THz, reaching nearly 100% in the vicinity of the conductivity minimum at high fields. The enhancement appears already at low magnetic fields and broadens progressively with increasing B , bounded by a 50% MR contour that expands to roughly 1 THz at 7 T. Outside this region the response remains comparatively weak, staying near zero for $B < 2$ T and reaching only $\sim 30\%$ at higher fields. A similar pattern persists at 50 K (Fig. 4b), although with reduced overall intensity, indicating that the terahertz MR remains substantial even above T_N . By contrast, at 120 K (Fig. 4c) the map is dominated by weak responses, with only a faint remnant of the cone-like structure visible and maximum values below $\sim 30\%$.

To facilitate comparison between the terahertz response and its zero-frequency extrapolation, Fig. 4(d) shows MR curves extracted from the maps at $\nu = 1.5$ THz together with the extrapolated dc MR. At both 1.6 K and 50 K the terahertz MR rises steeply at low fields and gradually approaches a saturation-like behavior at intermediate fields. At 7 T, $\text{MR}(\nu = 1.5 \text{ THz})$ reaches $\sim 93\%$ at 1.6 K and $\sim 89\%$ at 50 K, whereas the dc MR remains near $\sim 30\%$ and $\sim 20\%$, respectively.

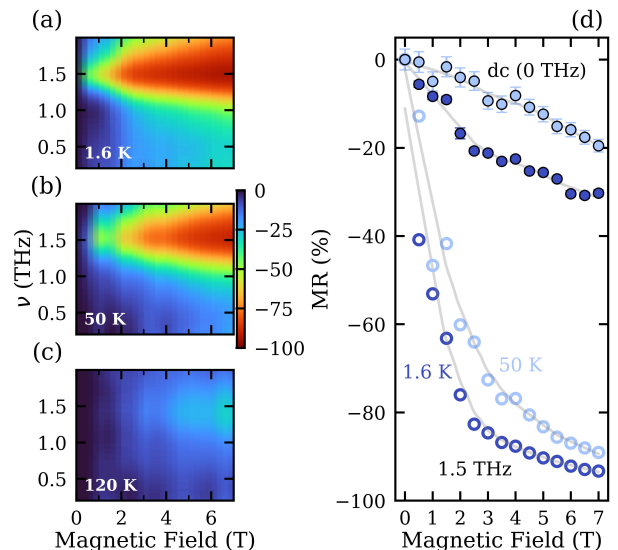


FIG. 4. (a–c) Terahertz magnetoresistance (%) as a function of magnetic field and frequency at $T = 1.6, 50$ and 120 K. (d) Field dependence of the terahertz magnetoresistance at dc (filled symbols) and at 1.5 THz (open symbols), for $T = 1.6$ K (dark blue) and 50 K (light blue). Solid lines are guides to the eye. Error bars are shown where visible; otherwise, they are smaller than the data point symbols.

This large disparity between terahertz and dc MR establishes a colossal terahertz magnetoresistance in EuZn_2P_2 , demonstrating that terahertz conductivity is exceptionally sensitive to field-induced changes in the electronic response associated with magnetic-polaron correlations.

Discussion—The observation of a colossal terahertz magnetoresistance in EuZn_2P_2 places our results in the broader context of large magnetoresistive phenomena that have attracted intense recent interest because of their fundamental importance and potential for magnetic control of electrical conductivity [34–41]. At terahertz frequencies, large magnetoresistive responses have been reported most prominently in manganites and, more recently, in spin-textured antiferromagnets. In manganites, negative THz MR have been measured in $\text{La}_{1-x}\text{Sr}_x\text{MnO}_3$, reaching about 40% in 8 T at 1 THz [42] and nearly 60% in 6 T at 0.4 THz [27], depending on composition, both near the Curie temperature. These effects have been discussed in terms of intrinsic intragrain transport associated with double exchange, hopping between localized states, and phase competition. Scaling relations between conductivity and terahertz dielectric permittivity have also been investigated in the CMR regime of $\text{Pr}_{0.65}\text{Ca}_{0.28}\text{Sr}_{0.07}\text{MnO}_3$ [43].

Similar to our observations, Ref. [42] reports a THz MR larger than the extrapolated dc value. Conversely, the discrepancy between the large dc CMR measured in transport experiments [16, 21] and the smaller MR inferred from the zero-frequency extrapolation of the THz

conductivity can be understood in terms of the different time and length scales probed by these techniques. While dc transport is sensitive to long-range conduction paths, terahertz spectroscopy probes local carrier dynamics and is therefore less affected by inhomogeneous transport or slow channels lying below the experimental frequency window. Additional differences may also arise from extrinsic effects such as electrical contacts.

More recently, giant negative THz MR in EuTe_2 was linked to a distinct mechanism based on magnetic-field control of spin orientation and the associated reconstruction of the low-energy band structure, including a field-induced gap change. In that system, MR exceeding 90 % was reported in 2.5 T at 1.1 THz for temperatures slightly above T_N [44]. In comparison, the terahertz MR observed here in EuZn_2P_2 reaches the same record level above 4 T near T_N , albeit at higher frequency, placing it among the largest responses reported to date. Importantly, the mechanism responsible for the effect is fundamentally different from those previously reported. Our results indicate a strong magnetoresistive response governed by magnetic polarons, demonstrating that polaronic magnetotransport remains active in terahertz frequencies for this class of correlated magnetic semiconductors.

Conclusions—In summary, our time-domain magnetospectroscopy measurements reveal that magnetic polarons strongly reshape the terahertz optical conductivity of the Eu-based Zintl antiferromagnet EuZn_2P_2 , producing a colossal negative terahertz magnetoresistance that exceeds 90 % at 1.5 THz near the magnetic transition temperature. The magnetoresistance at terahertz frequencies is roughly three times larger than the value inferred in the zero-frequency limit and becomes large already at moderate magnetic fields, demonstrating a pronounced frequency-dependent magnetotransport response. At the same time, the low-energy electronic response associated with magnetic polarons exhibits a maximum lifetime at the Néel temperature, highlighting the strong coupling between spin correlations and charge dynamics in this system. These results establish magnetic polarons as a key mechanism governing the terahertz electrodynamics of this class of correlated magnetic semiconductors. The substantial magnetic control of the polaronic terahertz conductivity observed here may also be of interest for magnetically tunable terahertz devices.

Acknowledgements—We acknowledge financial support from the São Paulo Research Foundation (FAPESP) under Grant Nos. 2021/12470-8, 2023/04245-0, and 2023/16742-8, and by the National Council for Scientific and Technological Development (CNPq) under Grant No. 306550/2023-7. E.M. acknowledges financial support from Grant No. 88887.007580/2024-00 of the Coordenação de Aperfeiçoamento de Pessoal de Nível Superior (CAPES). Additional support from the INCT Advanced

Quantum Materials project funded by CNPq (Grant No. 408766/2024-7), FAPESP (Grant No. 2025/27091-3), and CAPES is also gratefully acknowledged. Activities within the GMQ/UFABC group were supported by FAPESP under Grant No. 2017/10581-1, CNPq under Grant Nos. 309363/2022-5 and 405408/2023-4, CAPES, and CEM/UFABC.

Data availability—The data that support the findings of this article are available from the authors upon reasonable request.

* Corresponding author: felixggh@if.usp.br

- [1] P. Rosa, Y. Xu, M. Rahn, J. Souza, S. Kushwaha, L. Veiga, A. Bombardi, S. Thomas, M. Janoschek, E. Bauer, M. Chan, Z. Wang, J. Thompson, N. Harrison, P. Pagliuso, A. Bernevig, and F. Ronning, *npj Quantum Materials* **5**, 52 (2020).
- [2] Z.-C. Wang, J. D. Rogers, X. Yao, R. Nichols, K. Atay, B. Xu, J. Franklin, I. Sochnikov, P. Ryan, D. Haskel, and F. Tafti, *Advanced Materials* **33**, 2005755 (2021).
- [3] X. Chen, S. Dong, and Z.-C. Wang, *J. Phys. Condens. Matter* **37**, 033001 (2024).
- [4] S. Luo, Y. Xu, F. Du, L. Yang, Y. Chen, C. Cao, Y. Song, and H. Yuan, *Phys. Rev. B* **108**, 205140 (2023).
- [5] F. Tang, Y. Chen, W. Yu, Y. Chen, S. Wang, W. Zhao, X. Yin, Y. Liu, X. Zhang, Z. Han, and Y. Fang, *Phys. Rev. Mater.* **9**, 064205 (2025).
- [6] R. P. Day, K. Yamakawa, L. P. Cairns, J. Singleton, W. L. Cao, C. Wu, M. Allen, J. E. Moore, and J. G. Analytis, *Phys. Rev. B* **111**, 054406 (2025).
- [7] Z. Zhou, Z. Wang, X. Chen, J.-Y. Lu, J. Zhang, X. Luo, G.-H. Cao, S. Dong, and Z.-C. Wang, *Phys. Rev. Mater.* **8**, 114421 (2024).
- [8] J. C. Souza, S. M. Thomas, E. D. Bauer, J. D. Thompson, F. Ronning, P. G. Pagliuso, P. F. S. Rosa, and P. Rosa, *Phys. Rev. B* **105**, 035135 (2022).
- [9] M. Kopp, C. Garg, S. Krebber, K. Kliemt, C. Krellner, S. R. Balguri, M. Mahendru, F. Tafti, T. L. Breeze, N. P. Bentley, F. L. Pratt, T. J. Hicken, H. Luetkens, J. A. Krieger, S. J. Blundell, T. Lancaster, M. V. A. Crivillero, S. Wirth, and J. Müller, *npj Quantum Materials* **10.1038/s41535-026-00859-7** (2026).
- [10] M. Pohlit, S. Rößler, Y. Ohno, H. Ohno, S. von Molnár, Z. Fisk, J. Müller, and S. Wirth, *Phys. Rev. Lett.* **120**, 257201 (2018).
- [11] R. Ulbricht, E. Hendry, J. Shan, T. F. Heinz, and M. Bonn, *Rev. Mod. Phys.* **83**, 543 (2011).
- [12] C. C. Homes, Z.-C. Wang, K. Fruhling, and F. Tafti, *Phys. Rev. B* **107**, 045106 (2023).
- [13] M. Dutra, G. G. Vasques, P. C. Sabino, J. G. Dias, J. F. Oliveira, M. A. V. Heringer, M. Cabrera-Baez, E. B. Saitovitch, A. R. V. Benvenho, M. A. Avila, and J. Munevar, *Phys. Rev. Mater.* **10**, 016204 (2026).
- [14] T. Berry, V. J. Stewart, B. Y. Redemann, C. Lygouras, N. Varnava, D. Vanderbilt, and T. M. McQueen, *Phys. Rev. B* **106**, 054420 (2022).
- [15] S. Krebber, M. Kopp, C. Garg, K. Kummer, J. Sichelschmidt, S. Schulz, G. Poelchen, M. Mende,

- A. V. Virovets, K. Warawa, M. D. Thomson, A. V. Tarasov, D. Y. Usachov, D. V. Vyalikh, H. G. Roskos, J. Müller, C. Krellner, and K. Kliemt, *Phys. Rev. B* **108**, 045116 (2023).
- [16] M. S. Cook, E. A. Peterson, C. S. Kengle, E. R. Kennedy, J. Sheeran, C. Girod, G. S. Freitas, S. M. Greer, P. Abbamonte, P. G. Pagliuso, J. D. Thompson, S. M. Thomas, and P. F. S. Rosa, *Phys. Rev. Mater.* **9**, 104403 (2025).
- [17] A. Baydin, T. Makihara, N. M. Peraca, and J. Kono, *Front. Optoelectron.* **14**, 110 (2021).
- [18] M. Koch, D. M. Mittleman, J. Ornik, and E. Castro-Camus, *Nat. Rev. Methods Primers* **3** (2023).
- [19] E. D. Stefanato, N. M. Kawahala, B. A. Kawata, P. H. O. Rappl, E. Abramof, and F. G. G. Hernandez, *Commun. Phys.* **8** (2025).
- [20] D. N. Basov, R. D. Averitt, D. van der Marel, M. Dressel, and K. Haule, *Rev. Mod. Phys.* **83**, 471 (2011).
- [21] M. Dutra, E. Marulanda, G. G. Vasques, J. F. Oliveira, P. C. Sabino, R. B. Delgado, L. Mendonça-Ferreira, A. R. V. Benvenho, E. Baggio-Saitovitch, R. K. Machado, N. M. Kawahala, J. Munevar, M. A. Avila, and F. G. G. Hernandez, (2025), arXiv:2512.17123 [cond-mat.str-el].
- [22] See Supplemental Material at [URL will be inserted by publisher] for additional fit details and parameters.
- [23] D. Rybicki, K. Komędera, J. Przewoźnik, L. Gondek, C. Kapusta, K. Podgórska, W. Tabiś, J. Żukrowski, L. M. Tran, M. Babij, Z. Bukowski, L. Havela, V. Buturlim, J. Prchal, M. Divis, P. Kral, I. Turek, I. Halevy, J. Kastil, M. Mísek, U. Dutta, and D. Legut, *Phys. Rev. B* **110**, 014421 (2024).
- [24] U. Yu, J. Chatterjee, and B. I. Min, *Journal of Applied Physics* **97**, 10A903 (2005).
- [25] A. K. Jonscher, *Nature* **267**, 673 (1977).
- [26] S. R. Elliott, *Adv. Phys.* **36**, 135 (1987).
- [27] F. Tay, S. Chaudhary, J. He, N. M. Peraca, A. Baydin, G. A. Fiete, J. Zhou, and J. Kono, *Optica* **10**, 932 (2023).
- [28] Y. Zhang, K. Deng, X. Zhang, M. Wang, Y. Wang, C. Liu, J.-W. Mei, S. Kumar, E. F. Schwier, K. Shimada, C. Chen, and B. Shen, *Phys. Rev. B* **101**, 205126 (2020).
- [29] J. Y. Chan, S. M. Kauzlarich, P. Klavins, R. N. Shelton, and D. J. Webb, *Phys. Rev. B* **57**, R8103 (1998).
- [30] H. Dawczak-Dębicki, M. V. Ale Crivillero, M. S. Cook, S. M. Thomas, P. F. S. Rosa, J. Müller, U. K. Rößler, P. Schlottmann, and S. Wirth, *Commun. Mater.* **5**, 248 (2024).
- [31] D. Emin and M. S. Hillery, *Phys. Rev. B* **37**, 4060 (1988).
- [32] A. S. Alexandrov and A. M. Bratkovsky, *Journal of Physics: Condensed Matter* **11**, L531 (1999).
- [33] C. Hartinger, F. Mayr, A. Loidl, and T. Kopp, *Phys. Rev. B* **73**, 024408 (2006).
- [34] A. Rahman, M. U. Rehman, Y. Zhang, W. Zhao, J. Wang, Z. Chen, Z. Muhammad, and L. Zhang, *Phys. Rev. B* **110**, 064407 (2024).
- [35] F. Tang, Y. Chen, X. Yin, W. Zhao, L. Zhang, Z. Han, R. Zheng, X. Zhang, and Y. Fang, *Phys. Rev. B* **110**, 174408 (2024).
- [36] S. Karki Chhetri, G. Acharya, D. Graf, R. Basnet, S. Rahman, M. M. Sharma, D. Upreti, M. R. U. Nabi, S. Kryvyi, J. Sakon, M. Mortazavi, B. Da, H. Churchill, and J. Hu, *Phys. Rev. B* **111**, 014431 (2025).
- [37] S. Balguri, M. B. Mahendru, E. O. G. Delgado, K. Fruhling, X. Yao, D. E. Graf, J. A. Rodriguez-Rivera, A. A. Aczel, T. J. Hicken, H. Luetkens, M. J. Graf, A. Rydh, J. Gaudet, and F. Tafti, *Phys. Rev. B* **111**, 115114 (2025).
- [38] Q. Dong, P. Yang, Z. Liu, Y. Wang, H. Wen, Z. Liu, T. Shi, Z. Tian, J. Sun, Y. Uwatoko, Q. Wu, G. Chen, B. Wang, and J. Cheng, *Phys. Rev. B* **112**, L140405 (2025).
- [39] K. Singh, J. Skolimowski, G. Cuono, R. M. Sattigeri, A. Ptok, O. Pavlosiuk, T. Romanova, T. Toliński, P. Wiśniewski, C. Autieri, and D. Kaczorowski, *Phys. Rev. B* **112**, 134440 (2025).
- [40] M. S. Cook, B. R. Ortiz, P. Park, K. Gornicka, S. Sarker, J. Yan, and M. A. McGuire, *Phys. Rev. Mater.* **9**, 124410 (2025).
- [41] Y. Wang, Z. Liu, Y. Wang, C. Li, X. Wang, K. Liao, Q. Wu, and G. Wang, *Phys. Rev. B* **113**, 024425 (2026).
- [42] J. Lloyd-Hughes, C. D. W. Mosley, S. P. P. Jones, M. R. Lees, A. Chen, Q. X. Jia, E.-M. Choi, and J. L. MacManus-Driscoll, *Nano Letters* **17**, 2506 (2017).
- [43] A. Pimenov, M. Biberacher, D. Ivannikov, A. Loidl, A. A. Mukhin, Y. G. Goncharov, and A. M. Balbashov, *Physical Review B* **73**, 220407 (2006).
- [44] P. Hao, Z. Ren, B. Huang, X. Chang, Z. Xu, Y. Guo, Z. Zhong, X. Liu, and Z. Sheng, *ACS Applied Materials & Interfaces* **18**, 5467 (2026).
- [45] E. Marulanda, F. L. Costa, N. M. Kawahala, and F. G. G. Hernandez, *J. Infrared Millim. Terahertz Waves* **46** (2025).
- [46] J. Lloyd-Hughes and T.-I. Jeon, *J. Infrared Millim. Terahertz Waves* **33**, 871 (2012).

SUPPLEMENTARY MATERIAL

SAMPLES

High-purity single crystals of EuZn_2P_2 were synthesized by the Sn-flux method. High-purity elements, Eu (99.9%), Zn (99.999%), P (99.999%), and Sn (99.999%) from Alfa-Aesar were weighted in an atomic ratio of 1:2:2:40 and placed inside a quartz tube with quartz wool. The evacuated and sealed ampoule was gradually heated to 500 °C over 2 h, kept at this temperature for 1 h, then further heated to 1150 °C over 4 h and held at this temperature for 10 h. Controlled cooling was carried out down to 850 °C at a rate of 2 °C/h, after which the tubes were rapidly spun to separate the crystals from the flux. More details can be found in references [13, 21].

EXPERIMENTAL DETAILS

We performed terahertz time-domain spectroscopy (THz-TDS) measurements in transmission, using a commercial PCA-based time-domain spectrometer (TOPTICA). The spectrometer was coupled to a cryofree (Oxford Instruments Spectromag) superconducting magnet system. We measure the complex transmission coefficient $\tilde{T}(\nu) = |T(\nu)|e^{i\phi(\nu)}$ of EuZn_2P_2 samples by magneto THz-TDS in Faraday geometry. Following Ref. [45] and standard Fresnel inversion for a plane-parallel slab [46], we extract the complex optical conductivity $\tilde{\sigma}(\nu) = \sigma_1(\nu) + i\sigma_2(\nu)$. We focus our analysis on the dissipative component $\sigma_1(\nu)$: it is directly constrained by the measured attenuation, contains the key transport observables (spectral weight, relaxation rate) relevant to magnetic-polaron transport, and is experimentally more robust than $\sigma_2(\nu)$, which in bulk samples is particularly sensitive to small phase errors and thickness uncertainties.

SUPPLEMENTARY FIGURES

An Arrhenius analysis of the high-temperature THz conductivity in EuZn_2P_2 Fig. S1 yields an activation energy of $E_a/h = 3.5 \pm 0.3$ THz (≈ 14.5 meV). In the semilogarithmic representation of σ_1 at 1.5 THz versus inverse temperature, the data follow the activated form $\sigma_1(T) \propto \exp(-E_a/k_B T)$ over $60 \text{ K} \leq T \leq 150 \text{ K}$. The deviation from this behavior below $\sim 60 \text{ K}$ occurs well above the Néel temperature, $T_N = 23.5 \text{ K}$.

The fit parameters from $\sigma(\nu) = \sigma_p + A(\nu - \nu_0)^{2q}$ are shown as a function of temperature and magnetic field in Figs. S2 and S3, respectively.

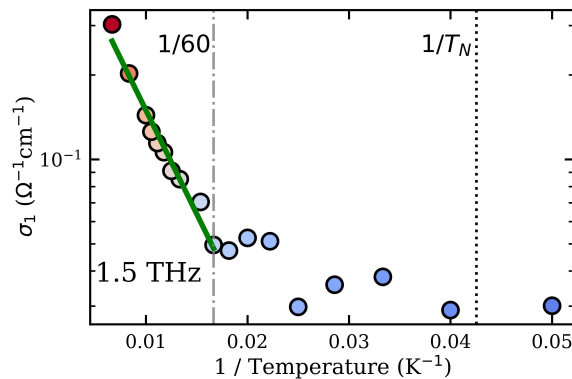


Fig. S1. Semilogarithmic plot of the real part of the optical conductivity, σ_1 , at 1.5 THz for EuZn_2P_2 as a function of inverse temperature. The dashed line is the Arrhenius fit over $60 \text{ K} \leq T \leq 150 \text{ K}$. The dot-dashed and dotted lines mark 60 K and $T_N = 23.5 \text{ K}$, respectively.

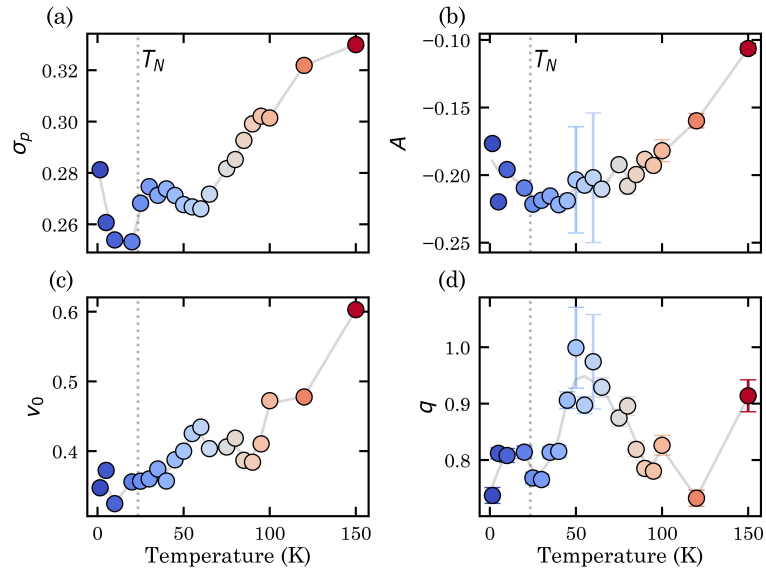


Fig. S2. Temperature dependence of the fit parameters: (a) σ_p , (b) A , (c) ν_0 , and (d) q . The vertical dotted line marks T_N . Solid lines are guides to the eye.

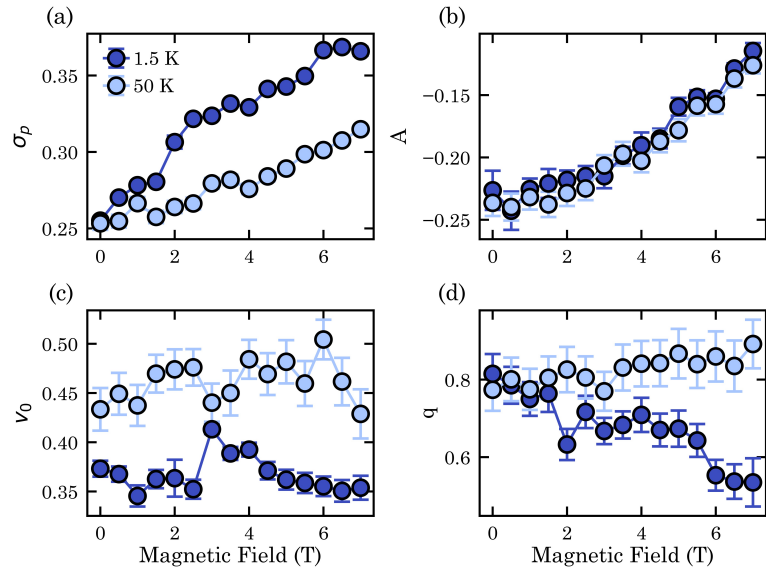


Fig. S3. Magnetic-field dependence of the fit parameters: (a) σ_p , (b) A , (c) ν_0 , and (d) q . Solid lines are guides to the eye.